science.sciencemag.org/content/366/6467/856/suppl/DC1

Supplementary Materials for

Widely tunable compact terahertz gas lasers

Paul Chevalier, Arman Amirzhan, Fan Wang, Marco Piccardo, Steven G. Johnson, Federico Capasso*, Henry O. Everitt*

*Corresponding author. Email: everitt@phy.duke.edu (H.O.E.); capasso@seas.harvard.edu (F.C.)

Published 15 November 2019, *Science* **366**, 856 (2019)
DOI: 10.1126/science.aay8683

This PDF file includes:

CONTENTS

I. MATERIALS AND METHODS

A. Tuning the QCL emission into the gas absorption line

External-Cavity (EC)-QCLs rely on a diffraction grating mounted on a precisely controlled actuator (piezo-electric, stepper-motor, voice-coil actuator). The laser device used in this paper (Daylight Solutions HHG 41045), is factory calibrated for grating tuning of the emission, but this tuning is discrete and typically has a resolution of 0.1 cm^{-1}. According to the manufacturer specifications, the target emission wavenumber and the actual emission wavenumber may differ by up to 1 cm^{-1}. Once the grating is tuned to a desired position, continuous tuning can occur by changing the temperature of the laser. For the experiments described here, tuning into an absorption line was performed as follows: a line is selected and the grating of the EC-QCL is tuned close to the HITRAN value for the transition, then the QCL temperature is cycled between 17 and 22°C while the transmitted intensity through the gas cell is monitored by a Vigo PV-106 HgCdTe detector. If during this cycling of the temperature a strong absorption feature was observed, the QCL temperature was finely adjusted in order to minimize the transmitted intensity. The emission wavenumber of the QCL was then measured on the FTIR and compared with HITRAN data to confirm that the targeted transition was effectively selected. If during the cycling of the QCL temperature no absorption feature was seen, then the grating was tuned by increments of 0.1 cm^{-1} until an absorption feature was observed.

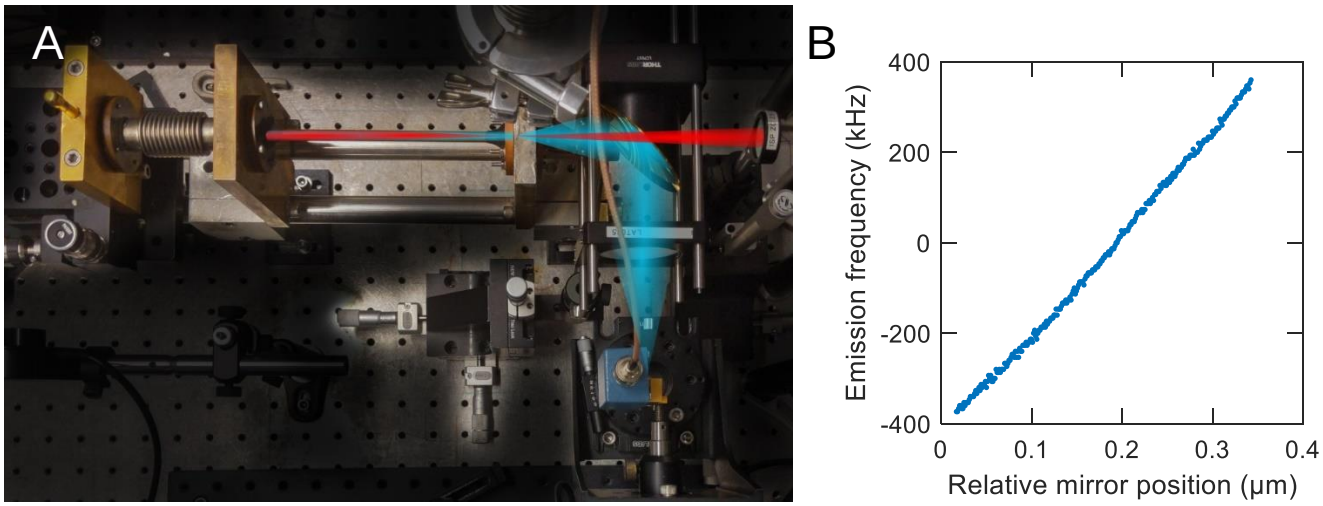

Figure S1. **A** Photograph of the experimental setup showing the different components of the laser cavity, the path of the QCL beam (red), and how the output light (blue) is collected. **B** Plot of the measured relative emission frequency of the THz gas laser as a function of the back-mirror position for $J_L = 10$, ($\nu_{\mathrm{THz}} \approx 0.299$ THz).

B. Controlling the pressure inside the THz laser cavity

The operating pressure range of the laser (Fig. S1A) lies between 10 mTorr and 100 mTorr (or 1.3 Pa to 13 Pa). To measure such low pressure levels in the cavity we use a Pirani pressure gauge (Alcatel sensor AP1004 and controller ACR1000) which has a resolution of 10^{-5} Torr and an accuracy of 10^{-3} Torr. To fill the cavity with a specific amount of gas, first a high vacuum (pressure below 10^{-5} Torr) is achieved in the cavity by using a Varian DS402 rough pump and a Varian V-70LP Turbo pump. A sample tube connected to the vacuum manifold with a valve and containing a few Torrs of pure nitrous oxide at atmospheric pressure is cooled down by a bath of liquid nitrogen (see schematic in Fig. 2A of the manuscript). Once high vacuum is reached in the cavity, nitrous oxide is introduced in the cavity by closing the vacuum pump valve, opening the valve of the sample tube and warming the tube and its contents. Since the liquid nitrogen bath has initially completely solidified the nitrous oxide in the tube, the sublimation of nitrous oxide will progressively increase the pressure in the cavity. The valve of the sample tube is closed when the proper pressure is reached in the cavity. To reduce the pressure in the cavity, nitrous oxide can be recycled into the sample tube by immersing it again in a bath of liquid nitrogen. This method allows for a slow rise of the pressure in the cavity and for reusing of the gas between experiments. Other methods, such as using a variable leak valve, would allow for precise pressure control but would not allow for reusing of the gas.

C. Measuring the THz laser output

Once the QCL was tuned into an absorption line and its emission frequency was confirmed, IR radiation passed through a hole in an off-axis parabolic mirror, through a ZnSe window at Brewster's angle, and through a 1 mm diameter pinhole into the laser cavity containing the molecular gas. Then, the back-mirror of the THz cavity was moved until lasing began and THz intensity was measured by the detector. Schottky diode detectors used for that purpose were Virginia Diodes, Inc. Zero Bias detectors (ZBD) with waveguide sizes WR3.4, WR2.2, WR1.5, WR1.2, and WR1.0 depending on the targeted emission frequency. The signal from the detector was amplified using a low-noise voltage amplifier (Stanford research SR560). The amplification factor was typically set between 5000 and 20,000.

The power output of the laser was measured using a calibrated power meter THZ5B-BL-DZ-D0 from Gentec electro-optics.

The spectral lines of the THz laser were measured using a receiver and mixer from Virginia Diodes. The WR2.2 receiver, covering 300 GHz to 550 GHz operated with a multiplier factor of 36 with a local oscillator (LO) power of 10 dBm. The WR1.5 receiver, covering 550 GHz to 775 GHz operated with a multiplier factor of 54 with an LO power of 15 dBm. The signal generator providing the LO signal was a Hittite HMC-T2240. The intermediate frequency (IF) was measured on an Agilent E4448A spectrum analyzer.

To obtain the molecular gain profile of the THz laser at a given pumped transition, the emission frequency of the laser was measured for different positions of the back-mirror. The free spectral range of the 15 cm long Fabry-Perot cavity is of the order of 1 GHz. As the relative position of the mirror increases, the length of the cavity decreases and the cavity mode ($\approx 10 - 100$ MHz

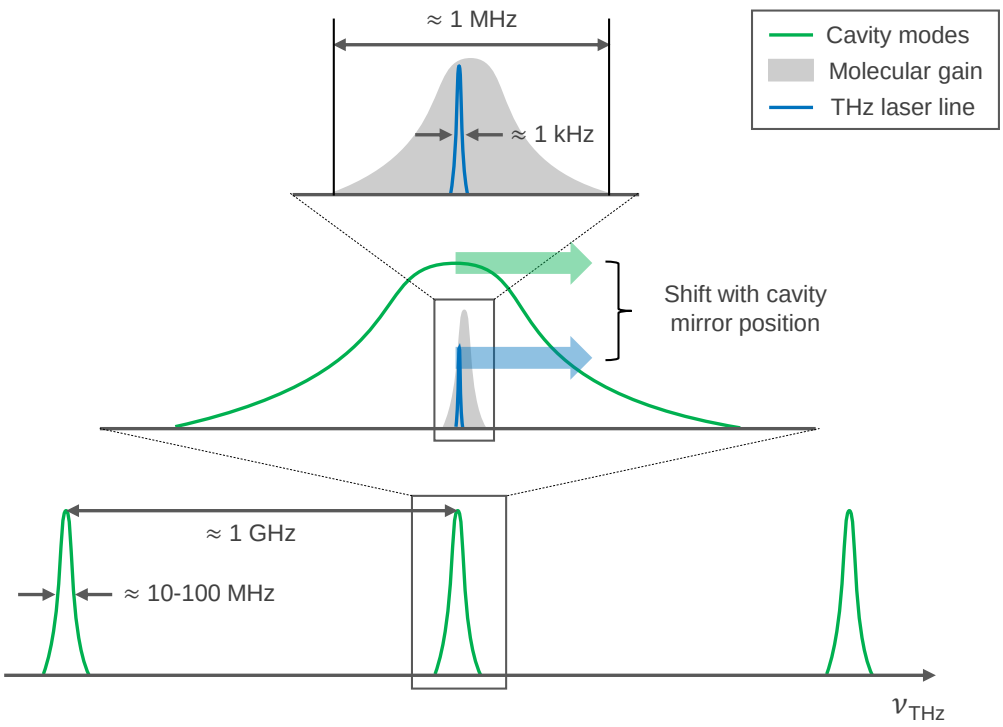

Figure S2. Schematic showing the tuning range of the THz laser for a given pumped transition. As the back-mirror of the gas cavity is translated, the free spectral range of the resonator is modified, resulting in a shift of the cavity modes. This in turn causes the emission frequency of the laser to shift within the frequency range of the molecular gain profile.

linewidth) is shifted toward higher frequencies (Fig. S2). This in turn shifts the laser frequency, to minimize the cavity losses and maximize the gain. In Fig. S1B, the emission frequency of the laser is plotted as a function of the position of the back-mirror. Since laser emission can only happen while a cavity mode overlaps with the gain profile of the pumped transition, this measurement gives the tuning range of the QPML ($\approx$ 1 MHz) for a given transition, as shown by the grey curve of Fig. 2E of the manuscript.

II. THEORETICAL MODELING

In the main text, a simple model is presented to describe the lasing behavior at low pressures with negligible intermolecular collisional transition rates. In order to fully understand the lasing behavior across all pressures, we have developed a more comprehensive model that thoroughly captures the collisional physics and can accurately predict the performance of QCL-pumped molecular lasers (QPMLs) [23]. In the model, rate equations of the population density of vibrational and rotational levels are solved numerically, and then the THz output power is computed based on the population inversions obtained from the rate equations when the QCL pump creates nonequilibrium populations.

For the N_2O laser, the model includes $J_L + 8$ rotational levels and the 10 lowest energy vibrational levels. The rate equations for the *rotational levels* are

$$\begin{aligned}\frac{dN_\ell(v,\mathbf{r},t)}{dt} = &\sum_{\ell'=\ell\pm1}\left[-\gamma_{\ell\ell'}N_\ell(v,\mathbf{r},t)+\gamma_{\ell'\ell}N_{\ell'}(v,\mathbf{r},t)\right]\\ &-\gamma_{\mathrm{SPT}}N_\ell(v,\mathbf{r},t)+R_{\mathrm{pump}}(v,\mathbf{r},t)+D\nabla^2N_\ell(v,\mathbf{r},t)\end{aligned} \tag{S1}$$

where $N_\ell(v,\mathbf{r},t)$ is the nonthermal population density for rotational level ℓ with axial velocity v along the pump beam direction, at position $\mathbf{r}$, and at time t, $\gamma_{\ell\ell'}$ is the dipole–dipole collisional transition rate. The thermal population density is calculated separately as part of the total population of a vibrational level, as described below. From the selection rules, ℓ' can only be $\ell \pm 1$. The transition rate is determined by $\gamma_{\ell\ell'} = n_{\mathrm{tot}}\langle v_{\mathrm{rel}}\rangle\sigma\rho_{\ell\ell'}$, where n_{tot} is the total molecular population density, $\langle v_{\mathrm{rel}}\rangle$ is the thermally averaged relative velocity, $\rho_{\ell\ell'}$ is the appropriate branching ratio with Boltzmann factor, and σ is the collisional cross section for the transition. In gas phase OPFIR lasers, the dominant collisional process is mediated by the dipole–dipole interaction, so that $\sigma \approx \sigma_{\mathrm{DD}}$. In the second line of Eq. (S1), $(-\gamma_{\mathrm{SPT}}N_\ell)$ describes the thermalization transition of rotational

level ℓ into its vibrational mode due to low energy collisions. The thermalization rate $\gamma_{\rm SPT}$ is computed from the gas kinetic cross section as $\sigma_{\rm GK} = 15\text{Å}^2$. $R_{\rm pump}$ describes the pump transition $J_L \rightarrow J_U$ thoroughly. It includes inhomogeneous broadening from different velocity subclasses with the Doppler effect, pressure broadening with HWHM equal to 4.0MHz/Torr, velocity-dependent saturation, and the multiple round-trips inside the cavity. The linewidth of the pump EC-QCL used in experiments is typically a few MHz. The detailed formula for $R_{\rm pump}$ can be found in Ref. 23. Diffusion is also included in the last term of Eq. (S1).

Similarly, the rate equations for the *vibrational levels* are

$$\begin{aligned}\frac{dN_p(v,\mathbf{r},t)}{dt} = &\sum_{p'=p\pm1}\left[-\gamma_{pp'}N_p(v,\mathbf{r},t)+\gamma_{p'p}N_{p'}(v,\mathbf{r},t)\right]\\ &+\Sigma_\ell\gamma_{\rm SPT}\int dvN_\ell(v,\mathbf{r},t)+D\nabla^2N_p(v,\mathbf{r},t)\end{aligned} \tag{S2}$$

in which $\gamma_{pp'}$ is the transition rate between vibrational levels $p \rightarrow p'$ and is assumed proportional to the gas kinetic cross section $\sigma_{\rm GK}$ and Boltzmann factor $\exp(-\Delta E_{pp'}/k_BT)$, where $\Delta E_{pp'}$ is the vibrational energy difference between p and p'. The last two terms describe the thermalization from rotational levels to vibrational levels as well as diffusion. The thermal population of a given rotational state is simply that state's fraction of the total thermal population in the corresponding vibrational level.

Molecule–wall collisions are modeled by a reaction boundary condition [23] so that wall collisions thermalize the vibrational levels and redistribute the molecules into all possible levels with a Boltzmann distribution at room temperature (300K). The ground vibrational state has the largest occupation probability.

We obtain the steady state by setting $dN/dt = 0$. These nonlinear rate equations are discretized and solved numerically by fixed-point iteration with Anderson Acceleration [23]. At each iteration step, MUMPS (MUltifrontal Massively Parallel sparse direct Solver [31]) is used for factorizing the sparse matrix.

THz output power is then obtained by matching the cavity loss $\alpha_{\rm cell}$ with the THz gain. In particular, the cavity loss includes Ohmic loss $\alpha_{\rm Ohmic}$ and transmission loss through the front window $\alpha_{\rm trans}$. Ohmic loss can be expressed analytically for the modes of a hollow metal waveguide, which increases strongly with decreasing radius [26]. The transmission loss is estimated by $\alpha_{\rm trans} = -\log(1-T)/2L$, where T is the front window transmission coefficient, and L is the cavity length. The gain coefficient is obtained by integrating contributions from all velocity subclasses. Detailed discussions and computational treatments can be found in Ref. 23.

III. DETERMINATION OF $\sigma_{\rm DD}$ AND OTHER PARAMETERS

Unlike widely-studied CH_3F, whose collisional parameters are experimentally well known [20, 21], many important collisional cross sections of N_2O are unknown, such as the most important $\sigma_{\rm DD}$ (dipole–dipole collisions). However, thanks to the completeness of our OPFIR model, we can use our experimental measurements of QMPL power as a function of pressure and QCL pump power to extract a few key unknowns by a fitting procedure. In particular, we use experimental fits to recover the dipole–dipole cross section $\sigma_{\rm DD}$, the cavity loss (since the alignment and other geometric factors were imperfectly known for our cavity), and the QCL linewidth. Our numerical modeling finds that the output power is insensitive to the gas kinetic collisional cross section, so $\sigma_{\rm GK}$ is fixed as 15Å^2, well within the expected range. Once these parameters were obtained, we could then proceed to use the model to predict other lasing behaviors and to identify the optimal cavity and operating regime.

Figure S3 shows the threshold power for the $J_L = 14$ direct lasing transition as a function of pressure for both experimental measurements (blue circles) and theoretical modeling (dashed lines) with different dipole–dipole cross sections $\sigma_{\rm DD} = 25\text{Å}^2$, 35Å^2, and 45Å^2. A reasonable range for $\sigma_{\rm DD}$ can be estimated by assuming $\sigma_{\rm DD}$ proportional to the dipole moment μ of the molecule. Consider $\mu_{\rm N_2O} = 0.17$ D, $\mu_{\rm CH_3F} = 1.8$ D, and $\sigma_{\rm DD}^{\rm CH_3F} = 320\text{Å}^2$, so $\sigma_{\rm DD}^{\rm N_2O} \approx \sigma_{\rm DD}^{\rm CH_3F}\frac{\mu_{\rm N_2O}}{\mu_{\rm CH_3F}} = 30\text{Å}^2$. Fig. S3 shows that $\sigma_{\rm DD} = 35\text{Å}^2$ gives the best agreement with experiments, which is also within the reasonable range. The cavity loss from the fitting is 0.3 $\rm m^{-1}$, which is about 5 times larger than an ideal cylindrical cavity operating on the TE_{01} mode. In principle, cavity loss can be computed with the exact cavity geometry and cavity mode. However, our current cavity has poor alignment using a concave back mirror with focal length about 2-3 cm, which easily couples the lasing mode to other cavity modes. In addition, the front pinhole coupler has a curved taper from the 1 mm diameter exit to the 5 mm diameter cavity, and this taper also contributes to mode mixing while suppressing long wavelength emission below cutoff. The QCL linewidth is fitted as 2 MHz to match Fig. 2C with Fig. 2D in the main text, a value that is well within the range previously reported for EC-QCLs [24].

Using the obtained collisional parameters, the theory–experiment match for $J_L = 31$ is also presented in Fig. S4. The agreement between theoretical modeling and experiments confirms the correctness of the deduced collisional cross sections and QCL linewidth. Only the cavity loss had to be adjusted, increased to 0.46 $\rm m^{-1}$ at this higher frequency to obtain good agreement. A frequency-dependent cavity loss is expected because of the increasing number of modes above cutoff at higher frequencies, which are coupled more easily to the lasing mode by the concave back plunger in our cavity with increasing J_L and lasing frequency. There is potential for improving the cavity design with a different geometry mirror or metasurface.

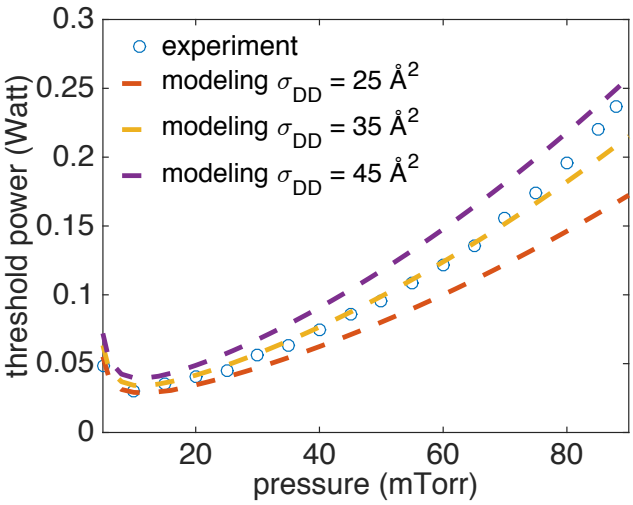

Figure S3. Threshold power for the direct lasing transition as a function of pressure for $J_L = 14$ or $\nu = 374$ GHz. Results from experimental measurement (blue circles) and theoretical modeling (dashed lines) with different values of $\sigma_{\rm DD} = 25$ Å^2, 35 Å^2, and 45 Å^2 are compared. In the model, the cavity loss is a fitting parameter (0.3 m^{-1}). The results imply that the dipole–dipole cross section of N_2O is $\sigma_{\rm DD} = 35$ Å^2.

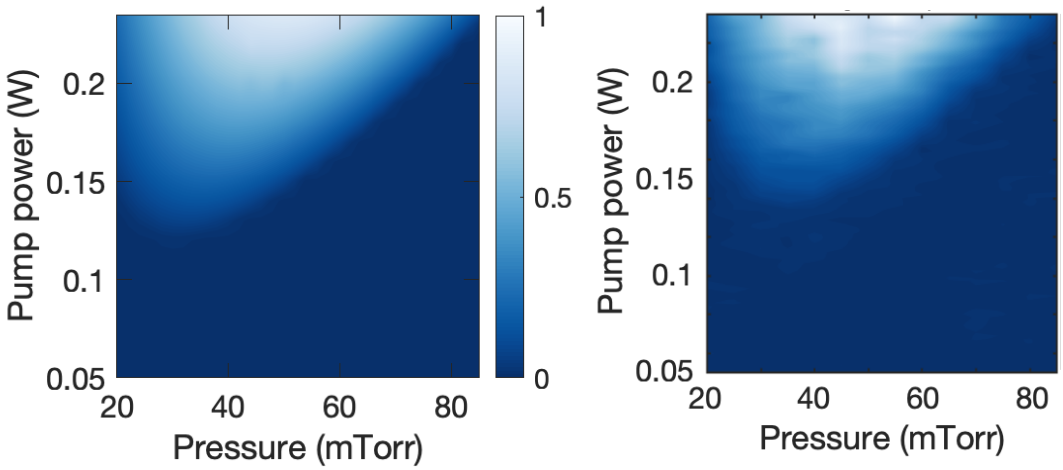

Figure S4. Contour plot of the THz output power from the $J_L = 31$ direct lasing transition at $\nu_{\rm THz} = 0.797$ THz as a function of pressure and pump power. The theoretical prediction (left) matches the experimental measurement (right) very well using the previously obtained dipole–dipole collisional cross section $\sigma_{\rm DD} = 35$ Å^2, and QCL linewidth of 2 MHz. The cavity loss is the only fitting parameter (0.46 m^{-1}).

IV. OUTPUT AND THRESHOLD POWER FOR DIFFERENT TRANSITIONS

Fig. S3 indicates that the pump threshold power increases with pressure, but this doesn't imply higher powers at lower pressures, because only a limited pressure-broadened velocity subclass fraction of the J_L population can be pumped. The optimal pressure with the highest output power occurs in between, as shown in Fig. S5 for both direct and refilling lasing with $J_L = 6$ ($\sim$ 175 GHz) to $J_L = 41$ ($\sim$ 1.05 THz). The peak powers for different transitions at the optimal pressures are plotted in the main text Fig. 3C. The comprehensive model predicts the direct transition with $J_L = 28$ produces the highest power. This is slightly different from the simple model prediction where the peak power appears for the transition with $J_L = 21$, as shown in Fig. 1B. The discrepancy is caused by the low pressure limitation of the simple model. In Fig. 1B, we fixed the gas pressure at 20 mTorr within the valid region of the simple model, while the comprehensive model implies that the optimal pressures are typically above 40 mTorr. In fact, Fig. S5A confirms that at 20 mTorr the transition with $J_L = 21$ has the highest power. Furthermore, lasing from direct inversion operates at higher pressures and with much more THz power than lasing from refilling inversion because the latter must overcome the effect of a much greater thermal population in the ground vibrational state that causes a greater threshold pump power.

Figure S6 shows the threshold power as a function of pressure for different direct transitions. $J_L = 30$ has the lowest threshold across all pressures above 40 mTorr where optimal pressure appears as shown in Fig. S5. This corresponds to the observation

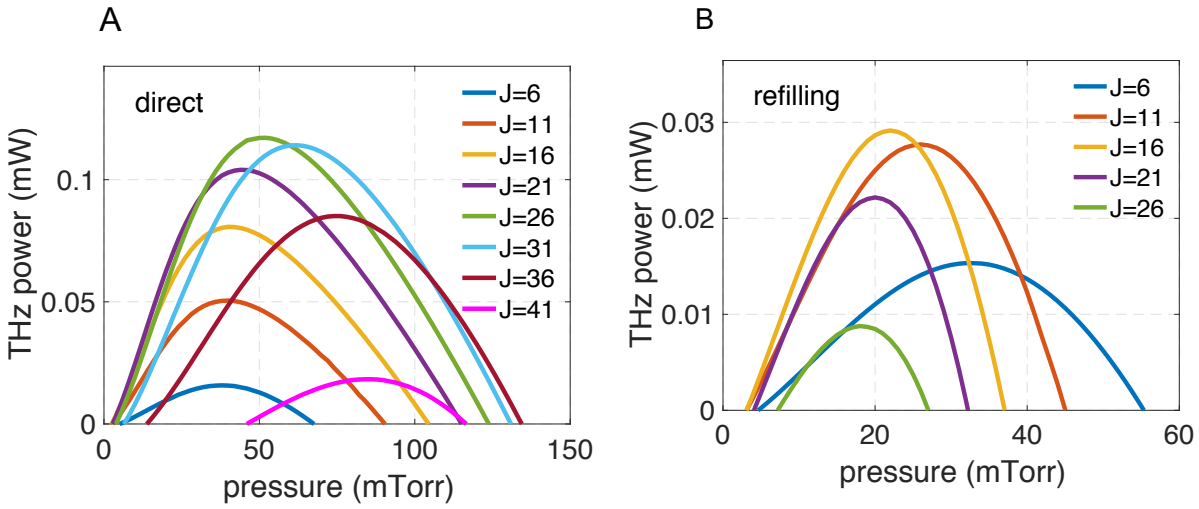

Figure S5. THz output power vs pressure with $J_L = 6$ to $J_L = 41$ for both direct and refilling lasing transitions.

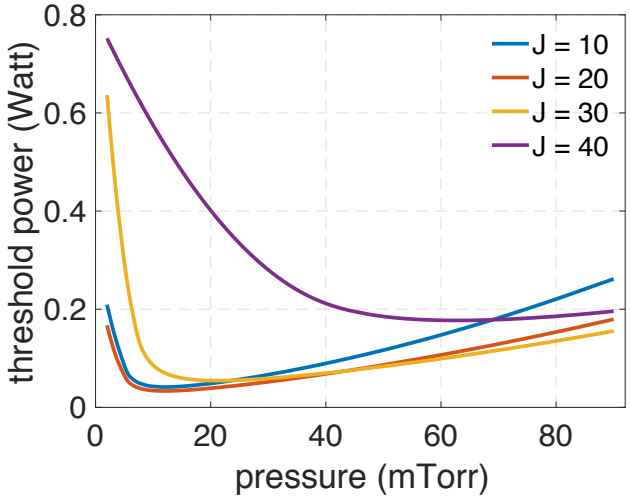

Figure S6. Pump threshold power as a function of pressure for $J_L = 10, 20, 30, 40$. The cavity loss is assumed to be 0.3m^{-1} for all cases.

in the main text (Fig. 3B) that $J_L = 28$ is predicted to produce the maximum power, even though the maximum population occurs at $J_L = 15$, because of the Manley–Rowe effect. A rotational state with J_L being either too large ($J_L = 40$) or too small ($J_L = 10$) has very limited population available to be pumped, therefore produces small gain to compensate the loss, leading to a high threshold. For $J_L = 40$, the threshold power increases with decreasing pressure below 60 mTorr. This is also an effect of a very limited population available to be pumped since the population fraction is only $n_{J=40} = 0.54\%$.

V. ANALYTICAL DERIVATION OF THRESHOLD AND OUTPUT POWERS

In a simplified three-level model as shown in Fig. S7, population in the ground level 1 is pumped with rate R_{pump} into level 2, followed by dipole–dipole collisions between level 2 and level 3 and collisions with the cavity wall. THz lasing occurs between level 2 and 3. Similar three-level models can be found in previous work [32–34], but were not designed to describe the behavior at very low pressures in very small cavities. Note that the spontaneous emission rate is not used for obtaining the population inversion, because in these collision-dominant molecular gas lasers the spontaneous emission rate ($1/t_{\text{sp}} \sim 10^{-5}s^{-1}$) is negligible compared with the dipole–dipole collision rate ($k_{\text{DD}} \sim 10^{5}s^{-1}$). The spontaneous emission rate between levels 2 and 3 is used only for the gain calculation. In this section, analytical derivations of the population inversion, gain coefficient, pump threshold, and the THz output power in the low-pressure limit are presented.

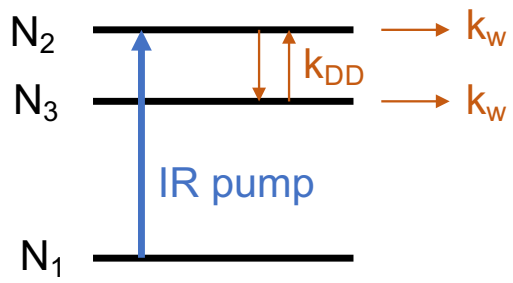

Figure S7. Schematics of a simplified three-level model for analytical derivations.

A. Pump threshold

Assuming molecular relaxation is dominated by molecule–wall collisions with rate k_w and intermolecular dipole–dipole collisions with rate k_{DD}, the rate equations for N_2 and N_3 are

$$\frac{dN_2}{dt} = R_{\mathrm{pump}} - N_2(k_{\mathrm{DD}} + k_w) + N_3 k_{\mathrm{DD}},$$
$$\frac{dN_3}{dt} = N_2 k_{\mathrm{DD}} - N_3(k_{\mathrm{DD}} + k_w)$$

At steady state, $dN_2/dt = dN_3/dt = 0$, and the population inversion is obtained as

$$\Delta N = N_2 - N_3 = \frac{R_{\mathrm{pump}}}{2k_{\mathrm{DD}} + k_w}. \tag{S3}$$

The pump rate can be approximated as

$$R_{\mathrm{pump}} = \frac{P_{\mathrm{QCL}}(\alpha_{\mathrm{IR}} L)}{h\nu_{\mathrm{IR}}} \frac{1}{\pi R_{\mathrm{cell}}^2 L} = \frac{\alpha_{\mathrm{IR}} P_{\mathrm{QCL}}}{\pi R_{\mathrm{cell}}^2 h\nu_{\mathrm{IR}}} \tag{S4}$$

in which α_{IR} is the infrared absorption coefficient of the gain medium, and R_{cell} and L are the cavity radius and length, respectively. The pump power absorbed by the gain medium is approximated as $P_{\mathrm{QCL}}(\alpha_{\mathrm{IR}} L)$.

The unsaturated gain coefficient is [35]

$$\gamma_0 = \sigma \Delta N = \left[\frac{\lambda^2}{8\pi^2 \Delta\nu t_{\mathrm{sp}}}\right] \Delta N$$

where σ is the cross section for the lasing transition, the spontaneous emission lifetime is $t_{\mathrm{sp}} = 3h\epsilon_0\lambda^3/16\pi^3\mu_{ij}^2$, where $\mu_{ij}^2 = |\langle i|\mu|j\rangle|^2$ is the dipole matrix element, and $\Delta\nu$ is the half width at half maximum of the gain profile approximated in this low pressure regime as the Doppler broadening half width $\Delta\nu \approx \Delta\nu_D \approx u/\lambda$, where u is the average absolute molecular velocity. With temperature T and molecular mass m, $u = \sqrt{8k_B T/\pi m}$. Then we obtain

$$\gamma_0 = \left(\frac{2}{3h^2\epsilon_0}\right)\left(\frac{\mu_{ij}^2}{u R_{\mathrm{cell}}^2}\right)\left(\frac{\alpha_{\mathrm{IR}} P_{\mathrm{QCL}}}{\nu_{\mathrm{IR}}}\right)\frac{1}{2k_{\mathrm{DD}} + k_w}. \tag{S5}$$

Threshold occurs when the unsaturated gain coefficient is equal to the cell loss, $\gamma_0 = \alpha_{\mathrm{cell}}$, and the threshold power can be derived as [35]

$$P_{\mathrm{th}} = \left(\frac{3h^2\epsilon_0\nu_{\mathrm{IR}}}{2}\right)\left(\frac{u R_{\mathrm{cell}}^2}{\mu_{ij}^2}\right)\left(\frac{\alpha_{\mathrm{cell}}}{\alpha_{\mathrm{IR}}}\right)(2k_{\mathrm{DD}} + k_w) \tag{S6}$$

At very low pressures in our very small cavity, where molecule–wall collisions dominate all other collisional processes, $k_w \gg k_{\mathrm{DD}}$, $k_w \approx 2u/3R$, and the pump threshold simplifies to

$$P_{\mathrm{th}} = \left(h^2\epsilon_0\nu_{\mathrm{IR}}\right)\left(\frac{u^2 R_{\mathrm{cell}}}{\mu_{ij}^2}\right)\left(\frac{\alpha_{\mathrm{cell}}}{\alpha_{\mathrm{IR}}}\right). \tag{S7}$$

The above derivations are in SI units. The dipole moment needs to be converted by $1\ \mathrm{Debye} = 3.33564 \times 10^{-30}\ \mathrm{C\,m}$. In Electrostatic CGS unit, Eq. (S7) is written as Eq. (2) in the main text by replacing ϵ_0 with $1/4\pi$.

B. THz output power

Output power is obtained by equating the saturated gain to the cavity loss,

$$\gamma = \frac{\gamma_0}{1+\Phi/\Phi_s} = \alpha_{\rm cell} \tag{S8}$$

in which Φ is the photon flux density that is proportional to THz output power $P_{\rm THz}$:

$$\begin{aligned} P_{\rm THz} &= \frac{1}{2} h\nu_{\rm THz} T(\pi R_{\rm cell}^2)\Phi \\ &= \frac{1}{2} h\nu_{\rm THz} T(\pi R_{\rm cell}^2)\left(\frac{\gamma_0}{\alpha_{\rm cell}} - 1\right)\Phi_s \end{aligned} \tag{S9}$$

where $R_{\rm cell}$ is the cavity radius, $\Phi_s = k_s \Delta N/\gamma_0$ is the saturated photon flux density, and T is the power transmission coefficient of the front coupler. For wavelengths smaller than the pinhole diameter $\lambda_{\rm THz} < 2r_0$, T can be approximated as $T \approx (\pi r_0/\pi R_{\rm cell})^2$, but if the lasing wavelength is larger than $2r_0$, T depends sensitively on the pinhole thickness. In the simple 3-level model, k_s can be derived as $k_s = (2k_{\rm DD} + k_w)/2$ following Ref. 35, and we obtain

$$\begin{aligned} P_{\rm THz} &= \frac{1}{2} h\nu_{\rm THz}(\pi r_0^2)\left(\frac{1}{\alpha_{\rm cell}} - \frac{1}{\gamma_0}\right)\frac{\alpha_{\rm IR} P_{\rm QCL}}{2\pi R_{\rm cell}^2 h\nu_{\rm IR}} \\ &= \frac{1}{4}\frac{\nu_{\rm THz}}{\nu_{\rm IR}}\frac{r_0^2}{R_{\rm cell}^2}\frac{\alpha_{\rm IR}}{\alpha_{\rm cell}}\left(1 - \frac{\alpha_{\rm cell}}{\gamma_0}\right) P_{\rm QCL} \\ &= \frac{1}{4}\frac{\nu_{\rm THz}}{\nu_{\rm IR}}\frac{r_0^2}{R_{\rm cell}^2}\frac{\alpha_{\rm IR}}{\alpha_{\rm cell}}\left(P_{\rm QCL} - P_{\rm th}\right). \end{aligned} \tag{S10}$$

Relationship $P_{\rm th}/\alpha_{\rm cell} = P_{\rm QCL}/\gamma_0$ is used in the above derivation. The power efficiency equals the derivative of $P_{\rm THz}$ with respect to the pump power:

$$\eta = \frac{1}{4}\frac{\nu_{\rm THz}}{\nu_{\rm IR}}\frac{r_0^2}{R_{\rm cell}^2}\frac{\alpha_{\rm IR}}{\alpha_{\rm cell}}. \tag{S11}$$

Here are a few direct observations. The output power and power efficiency are proportional to the IR absorption coefficient $\alpha_{\rm IR}$. Since $\alpha_{\rm IR}$ is proportional to the molecular pressure p and the population fraction of rotational level J_L, we have $P_{\rm THz}, \eta \propto \alpha_{\rm IR} \propto p\, n_{J_L}$. The output power and power efficiency are also proportional to the THz frequency, i.e., $P_{\rm THz}, \eta \propto \nu_{\rm THz}/\nu_{\rm IR}$, which is the Manley–Rowe effect.

In this derivation, it was assumed that the linewidth of the QCL was much narrower than the Doppler width of the pumped infrared transition, and indeed this is the case. Our experimental QCL is specified by the manufacturer to have a linewidth in the range of 1-10 MHz, also confirmed by other measurements [24], compared to the 50-150 MHz linewidth of typical molecular infrared transitions. Our analysis finds excellent agreement with the experimental results for a QCL linewidth of 2 MHz. If the QCL linewidth were larger, the simple model derived here could reflect this fact by using an averaged $\alpha_{\rm IR}$, obtained by a convolution of the QCL and Doppler lineshapes, rather than using the above approximation of $\alpha_{\rm IR}$ at its center frequency. Regarding the linewidth of the QPML laser transition, these lasers are perhaps more appropriately called "masers" [36] because their cavity linewidths (≈10-100 MHz) are larger than the molecular gain profile (≈1 MHz).

VI. USING AMMONIA (NH_3) AS A QPML GAIN MEDIUM

The oblate molecule ammonia (NH_3) combines many of the most attractive attributes for QPML operation: a low lying vibrational mode with a strong IR absorption coefficient and a large permanent dipole moment. Consequently, the simple model predicts that it will have low threshold and high power efficiency, attributes that should produce the strongest lines of the nine molecules considered here. Note that unlike the ground state inversion, which occurs at a relatively low frequency of 24 GHz, the inversion splitting in $v_2 = 1$ vibrational mode near 950 cm^{-1} is much larger, approximately 1 THz. Figure S8 plots the predicted laser lines for the strongest pure inversion and rotation-inversion transitions in NH_3, spanning transitions up to J = 9 excited by Q-branch transitions between 930 - 936 cm^{-1} and 962 - 968 cm^{-1}. The strongest laser lines are those for which J=K or K-1. Operation on several of pure-inversion lines near 1 THz has recently been experimentally shown [14] but the limited tuning range of pure inversion transitions minimizes the effectiveness of the Manley-Rowe factor.

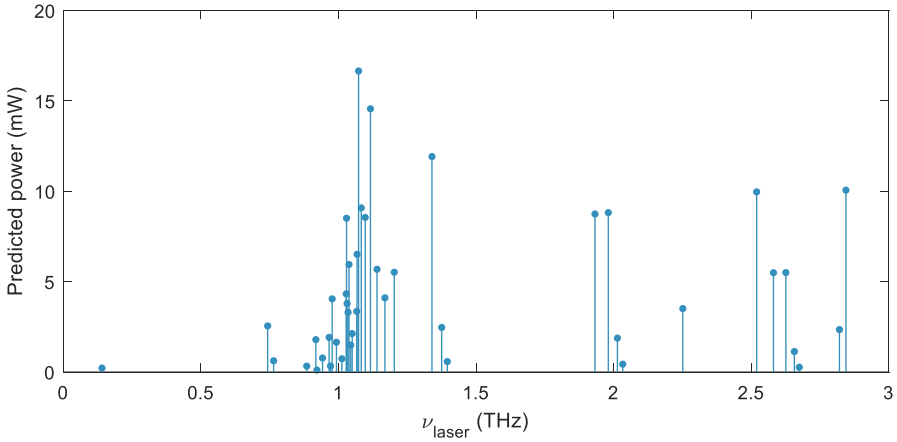

Figure S8. Plot showing the emission frequency and power predicted by the simple model for 20 mTorr of ammonia in a compact cylindrical cavity pumped by a 0.25 W QCL for emission frequency between 0 and 3 THz.

References and Notes

1. T. Nagatsuma, G. Ducournau, C. C. Renaud, Advances in terahertz communications accelerated by photonics. *Nat. Photonics* **10**, 371–379 (2016). doi:10.1038/nphoton.2016.65

2. R. A. Lewis, A review of terahertz sources. *J. Phys. D Appl. Phys.* **47**, 374001 (2014). doi:10.1088/0022-3727/47/37/374001

3. A. Maestrini, J. S. Ward, J. J. Gill, C. Lee, B. Thomas, R. H. Lin, G. Chattopadhyay, I. Mehdi, A frequency-multiplied source with more than 1 mW of power across the 840–900-GHz band. *IEEE Trans. Microw. Theory Tech.* **58**, 1925–1932 (2010). doi:10.1109/TMTT.2010.2050171

4. J. H. Booske, R. J. Dobbs, C. D. Joye, C. L. Kory, G. R. Neil, G.-S. Park, J. Park, R. J. Temkin, Vacuum electronic high power terahertz sources. *IEEE Trans. Terahertz Sci. Technol.* **1**, 54–75 (2011). doi:10.1109/TTHZ.2011.2151610

5. Y. Shen, P. Upadhya, E. Linfield, H. Beere, A. Davies, Ultrabroadband terahertz radiation from low-temperature-grown GaAs photoconductive emitters. *Appl. Phys. Lett.* **83**, 3117–3119 (2003). doi:10.1063/1.1619223

6. K. McIntosh, E. R. Brown, K. B. Nichols, O. B. McMahon, W. F. DiNatale, T. M. Lyszczarz, Terahertz photomixing with diode lasers in low-temperature-grown GaAs. *Appl. Phys. Lett.* **67**, 3844–3846 (1995). doi:10.1063/1.115292

7. K. Evenson, D. Jennings, F. Petersen, Tunable far-infrared spectroscopy. *Appl. Phys. Lett.* **44**, 576–578 (1984). doi:10.1063/1.94845

8. M. Inguscio, P. D. Natale, L. Veseth, *Comments At. Mol. Phys.* **30**, 3 (1994).

9. R. Köhler, A. Tredicucci, F. Beltram, H. E. Beere, E. H. Linfield, A. G. Davies, D. A. Ritchie, R. C. Iotti, F. Rossi, Terahertz semiconductor-heterostructure laser. *Nature* **417**, 156–159 (2002). doi:10.1038/417156a Medline

10. L. Bosco, M. Franckié, G. Scalari, M. Beck, A. Wacker, J. Faist, Thermoelectrically cooled THz quantum cascade laser operating up to 210 K. *Appl. Phys. Lett.* **115**, 010601 (2019). doi:10.1063/1.5110305

11. C. A. Curwen, J. L. Reno, B. S. Williams, Broadband continuous single-mode tuning of a short-cavity quantum-cascade VECSEL. *Nat. Photonics* 10.1038/s41566-019-0518-z (2019). doi:10.1038/s41566-019-0518-z

12. T. Chang, T. Bridges, E. Burkhardt, Submillimeter laser action in optically pumped methyl fluoride, methyl alcohol, and vinyl chloride gases. *Appl. Phys. Lett.* **17**, 249–251 (1970). doi:10.1063/1.1653386

13. J. Faist, F. Capasso, D. L. Sivco, C. Sirtori, A. L. Hutchinson, A. Y. Cho, Quantum cascade laser. *Science* **264**, 553–556 (1994). doi:10.1126/science.264.5158.553 Medline

14. A. Pagies, G. Ducournau, J.-F. Lampin, Low-threshold terahertz molecular laser optically pumped by a quantum cascade laser. *APL Photonics* **1**, 031302 (2016). doi:10.1063/1.4945355

15. I. Gordon, L. S. Rothman, C. Hill, R. V. Kochanov, Y. Tan, P. F. Bernath, M. Birk, V. Boudon, A. Campargue, K. V. Chance, B. J. Drouin, J.-M. Flaud, R. R. Gamache, J. T. Hodges, D. Jacquemart, V. I. Perevalov, A. Perrin, K. P. Shine, M.-A. H. Smith, J. Tennyson, G. C. Toon, H. Tran, V. G. Tyuterev, A. Barbe, A. G. Császár, V. M. Devi, T. Furtenbacher, J. J. Harrison, J.-M. Hartmann, A. Jolly, T. J. Johnson, T. Karman, I. Kleiner, A. A. Kyuberis, J. Loos, O. M. Lyulin, S. T. Massie, S. N. Mikhailenko, N. Moazzen-Ahmadi, H. S. P. Müller, O. V. Naumenko, A. V. Nikitin, O. L. Polyansky, M. Rey, M. Rotger, S. W. Sharpe, K. Sung, E. Starikova, S. A. Tashkun, J. V. Auwera, G. Wagner, J. Wilzewski, P. Wcisło, S. Yu, E. J. Zak, The HITRAN2016 molecular spectroscopic database. *J. Quant. Spectrosc. Radiat. Transf.* **203**, 3–69 (2017). doi:10.1016/j.jqsrt.2017.06.038

16. JPL Molecular Spectroscopy Database (2017); https://spec.jpl.nasa.gov/.

17. Splatalogue Database for Astronomical Spectroscopy (2007); http://www.cv.nrao.edu/php/splat/.

18. C. Townes, A. L. Schawlow, *Microwave Spectroscopy* (Dover Publications, 1995).

19. W. Gordy, R. L. Cook, *Microwave Molecular Spectroscopy* (Wiley-Interscience, 1984).

20. H. O. Everitt, D. D. Skatrud, F. C. DeLucia, Dynamics and tunability of a small optically pumped cw far-infrared laser. *Appl. Phys. Lett.* **49**, 995–997 (1986). doi:10.1063/1.97469

21. R. McCormick, H. Everitt, F. DeLucia, D. Skatrud, Collisional energy transfer in optically pumped far-infrared lasers. *IEEE J. Quantum Electron.* **23**, 2069–2077 (1987). doi:10.1109/JQE.1987.1073302

22. S.-L. Chua, C. A. Caccamise, D. J. Phillips, J. D. Joannopoulos, M. Soljacić, H. O. Everitt, J. Bravo-Abad, Spatio-temporal theory of lasing action in optically-pumped rotationally excited molecular gases. *Opt. Express* **19**, 7513–7529 (2011). doi:10.1364/OE.19.007513 Medline

23. F. Wang, J. Lee, D. J. Phillips, S. G. Holliday, S.-L. Chua, J. Bravo-Abad, J. D. Joannopoulos, M. Soljačić, S. G. Johnson, H. O. Everitt, A high-efficiency regime for gas-phase terahertz lasers. *Proc. Natl. Acad. Sci. U.S.A.* **115**, 6614–6619 (2018). doi:10.1073/pnas.1803261115 Medline

24. K. Knabe, P. A. Williams, F. R. Giorgetta, C. M. Armacost, S. Crivello, M. B. Radunsky, N. R. Newbury, Frequency characterization of a swept- and fixed-wavelength external-cavity quantum cascade laser by use of a frequency comb. *Opt. Express* **20**, 12432–12442 (2012). doi:10.1364/OE.20.012432 Medline

25. See supplementary materials.

26. R. Bansal, *Fundamentals of Engineering Electromagnetics* (CRC Press, 2006).

27. J. Manley, H. Rowe, Some general properties of nonlinear elements-Part I. General energy relations. *Proceedings of the IRE* **44**, 904–913 (1956). doi:10.1109/JRPROC.1956.275145

28. H. O. Everitt, F. C. De Lucia, Rotational energy transfer in small polyatomic molecules. *Adv. At. Mol. Opt. Phys.* **35**, 331–400 (1995). doi:10.1016/S1049-250X(08)60166-4

29. R. M. Williams, J. F. Kelly, J. S. Hartman, S. W. Sharpe, M. S. Taubman, J. L. Hall, F. Capasso, C. Gmachl, D. L. Sivco, J. N. Baillargeon, A. Y. Cho, Kilohertz linewidth from frequency-stabilized mid-infrared quantum cascade lasers. *Opt. Lett.* **24**, 1844–1846 (1999). doi:10.1364/OL.24.001844 Medline

30. R. L. Crownover, H. O. Everitt, F. C. De Lucia, D. D. Skatrud, Frequency stability and reproducibility of optically pumped far-infrared lasers. *Appl. Phys. Lett.* **57**, 2882–2884 (1990). doi:10.1063/1.103765

31. P. R. Amestoy, I. S. Duff, J.-Y. L'excellent, Multifrontal parallel distributed symmetric and unsymmetric solvers. *Comput. Methods Appl. Mech. Eng.* **184**, 501–520 (2000). doi:10.1016/S0045-7825(99)00242-X

32. R. J. Temkin, D. R. Cohn, Rate equations for an optically-pumped, far infrared laser. *Optics Communications* **16**, 213–217 (1976). doi:10.1016/0030-4018(76)90220-0

33. R. Panock, R. Temkin, Interaction of two laser fields with a three-level molecular system. *IEEE J. Quantum Electron.* **13**, 425–434 (1977). doi:10.1109/JQE.1977.1069354

34. D. A. McQuarrie, J. D. Simon, *Physical Chemistry: A Molecular Approach* (University Science Books, 1997).

35. B. E. A. Saleh, M. C. Teich, *Fundamentals of Photonics*, vol. 22 of *Wiley Series in Pure and Applied Optics* (Wiley, 1991).

36. A. L. Schawlow, C. H. Townes, Infrared and optical masers. *Phys. Rev.* **112**, 1940–1949 (1958). doi:10.1103/PhysRev.112.1940